AIAA JOURNAL
Vol. 55, No. 4, April 2017

Development of Compressible Large-Eddy Simulations Combining High-Order Schemes and Wall Modeling

S. Le Bras*
Centre Européen de Recherche et de Formation Avancée en Calcul Scientifique, 31057 Toulouse, France
H. Deniau†
ONERA — The French Aerospace Lab, 31000 Toulouse, France
C. Bogey‡
École Centrale de Lyon, 69134 Ecully, France
and
G. Daviller§
Centre Européen de Recherche et de Formation Avancée en Calcul Scientifique, 31057 Toulouse, France

DOI: 10.2514/1.J055107

Compressible large-eddy simulations combining high-order methods with a wall model have been developed in order to compute wall-bounded flows at high Reynolds numbers. The high-order methods consist of low-dissipation and low-dispersion implicit finite volume schemes for spatial discretization on structured grids. In the first part, the procedure used to apply these schemes in near-wall regions is presented. It is based on a ghost cell reconstruction. Its validity is assessed by performing the large-eddy simulation of a turbulent channel flow at a friction Reynolds number of $Re_\tau = 395$. In the second part, to consider flows at higher Reynolds numbers, a large-eddy simulation approach using a wall model is proposed. The coupling between the wall model and the high-order schemes is described. The performance of the approach is evaluated by simulating a turbulent channel flow at $Re_\tau = 2000$ using meshes with grid spacings of $\Delta x^+ = 100$, 200, and 300 in the streamwise direction and $\Delta^+ = 50$, 100, and 150 in the wall-normal and spanwise directions (in wall units). The effects of the choice of the point used for data exchange between the wall model and the large-eddy simulation algorithm, as well as of the positions of the ghost cells used for the coupling, are examined by performing additional computations in which these parameters vary. The results are in agreement with direct numerical simulation data. In particular, the turbulent intensities obtained in the logarithmic region of the boundary layers of the channel flow are successfully predicted.

I. Introduction

IN COMPUTATIONAL aeroacoustics, the direct calculation of the acoustic field from the Navier–Stokes equations requires accurate numerical methods to capture noise sources in turbulent flows and to propagate sound waves. Among various approaches available in the literature [1], the large-eddy simulation (LES) using high-order low-dissipation and low-dispersion schemes is an attractive way. In the LES approach, the large structures of the flows are computed, whereas the effects of the smallest turbulent scales are taken into account by a subgrid-scale model. Using high-order implicit schemes for spatial discretization offers the advantage of resolving the flow over a wide range of length scales using a reduced number of grid points. However, for wall-bounded flows at high Reynolds numbers (typically for $Re_L \geq 10^6$, where Re_L is the Reynolds number based on an integral flow scale L), the LES requires very fine grids to capture the small but dynamically important turbulent structures developing in the near-wall regions. These constraints on the grid resolution lead to computational costs that increase [2] with the Reynolds number as $Re_L^{13/7}$. In addition, according to the estimations of Piomelli and Balaras [3], to ensure the resolution of a boundary layer at $Re_L = 10^6$, around 99% of the grid points should be contained in the inner region of the boundary layer located between the wall and a distance corresponding to 20% of the boundary-layer thickness δ. Consequently, the LES of flows in the presence of walls with realistic geometries is out of reach using current numerical resources.

To perform LESs of wall-bounded flows at high Reynolds numbers, one solution consists of using a wall model in the near-wall regions instead of resolving the boundary layers. Wall modeling aims to reproduce the variations of the mean flow in the inner part of boundary layers by imposing approximate boundary conditions close to the walls. In that way, the LES can be performed on coarse grids that do not resolve the near-wall fluctuations. Consequently, the computational grid size is drastically reduced with respect to wall-resolved LESs. Wall modeling for the LES appeared in the 1970s in Deardorff's (1970) [4] and Schumann's (1975) [5] works, and it still knows great success among the scientific community [6]. In recent years, wall models have been applied to different flow configurations and implemented using several numerical approaches. In particular, the quality of LESs combining wall models and high-order methods has been examined by many authors. For instance, very promising results have been obtained using finite difference approaches [7] and spectral difference methods [8].

In this study, a compressible wall model [9] is combined with sixth-order finite volume compact schemes for spatial discretization in order to perform LESs of wall-bounded flows at high Reynolds numbers. The LES approach is based on the use of a selective filter as a subgrid-scale model. The present paper is organized as follows. In the first part, a procedure is proposed to apply the compact schemes near the walls. The procedure is validated for a turbulent channel flow at a low Reynolds number, with boundary-layer resolution at the wall.

Presented as Paper 2015-3135 at the 21st AIAA/CEAS Aeroacoustics Conference, Dallas, TX, 22–26 June 2015; received 9 February 2016; revision received 8 September 2016; accepted for publication 16 December 2016; published online 16 March 2017.

*lebras@cerfacs.fr (Corresponding Author).
†ONERA Research Scientist.
‡CNRS Research Scientist, Laboratoire de Mécanique des Fluides et d'Acoustique, UMR CNRS 5509; also Université de Lyon.
§Senior Researcher.

In the second part, to deal with flows at higher Reynolds numbers, the combination of the wall model with the high-order schemes is presented. The influence of the parameters used for wall modeling is investigated. In particular, the choice of the point where data are exchanged between the LES solver and the wall model is discussed. In addition, the importance of the positions of the ghost cells used to apply the selective filter near the wall is studied. The validity of the approach is finally examined for a turbulent channel flow with different spatial resolutions.

II. Wall-Resolved Simulations

A. Numerical Approach

1. Governing Equations

In the present work, the fully compressible three-dimensional Navier–Stokes equations are solved. In Cartesian coordinates, they can be written as follows:

$$\frac{\partial \boldsymbol{U}}{\partial t}+\frac{\partial \boldsymbol{E}_c}{\partial x}+\frac{\partial \boldsymbol{F}_c}{\partial y}+\frac{\partial \boldsymbol{G}_c}{\partial z}-\frac{\partial \boldsymbol{E}_d}{\partial x}-\frac{\partial \boldsymbol{F}_d}{\partial y}-\frac{\partial \boldsymbol{G}_d}{\partial z}=0 \tag{1}$$

where $\boldsymbol{U}=(\rho,\rho u,\rho v,\rho w,\rho e)^t$ is the variable vector; (u, v, w) are the velocity components; ρ is the density; ρe represents the total energy; $\boldsymbol{E}_c$, $\boldsymbol{F}_c$, and $\boldsymbol{G}_c$ are the convective fluxes; and $\boldsymbol{E}_d$, $\boldsymbol{F}_d$, and $\boldsymbol{G}_d$ are the diffusive fluxes. The total energy ρe for a perfect gas is defined by

$$\rho e=\frac{p}{\gamma-1}+\frac{1}{2}\rho(u^2+v^2+w^2) \tag{2}$$

where γ is the specific heat ratio, and p is the static pressure. The convective fluxes are given by

$$\begin{cases}\boldsymbol{E}_c=(\rho u,\rho u^2+p,\rho uv,\rho uw,(\rho e+p)u)^t\\ \boldsymbol{F}_c=(\rho v,\rho uv,\rho v^2+p,\rho vw,(\rho e+p)v)^t\\ \boldsymbol{G}_c=(\rho w,\rho uw,\rho vw,\rho w^2+p,(\rho e+p)w)^t\end{cases} \tag{3}$$

and the diffusive fluxes are given by

$$\begin{cases}\boldsymbol{E}_d=(0,\tau_{11},\tau_{12},\tau_{13},\tau_{11}u+\tau_{12}v+\tau_{13}w+\Phi_1)^t\\ \boldsymbol{F}_d=(0,\tau_{21},\tau_{22},\tau_{23},\tau_{21}u+\tau_{22}v+\tau_{23}w+\Phi_2)^t\\ \boldsymbol{G}_d=(0,\tau_{31},\tau_{32},\tau_{33},\tau_{31}u+\tau_{32}v+\tau_{33}w+\Phi_3)^t\end{cases} \tag{4}$$

where $\tau_{i,j}$ is the viscous stress tensor, and $\boldsymbol{\Phi}=(\Phi_1,\Phi_2,\Phi_3)^t$ is the heat flux vector. The viscous stress tensor $\tau_{i,j}$ is defined by $\tau_{i,j}=2\mu S_{i,j}$, where μ is the dynamic molecular viscosity and $S_{i,j}$ is the deformation stress tensor:

$$S_{i,j}=\frac{1}{2}\left(\frac{\partial u_i}{\partial x_j}+\frac{\partial u_j}{\partial x_i}-\frac{2}{3}\frac{\partial u_k}{\partial x_k}\delta_{i,j}\right) \tag{5}$$

The heat flux vector $\boldsymbol{\Phi}$ is computed using Fourier's law, yielding $\boldsymbol{\Phi}=-\lambda\nabla T$, where ∇T is the temperature gradient, $\lambda=C_p\mu/Pr$ is the thermal conductivity, C_p is the specific heat at constant pressure, and Pr is the Prandtl number.

2. Finite Volume Approach and High-Order Numerical Schemes

The computations are performed using the elsA software [10], which is a finite volume multiblock structured solver. Direct numerical simulations (DNSs) or large-eddy simulations can be carried out. In a finite volume approach, the computational domain is partitioned into nonoverlapping control volumes $\Omega_{i,j,k}$, where i, j, and k are the volume indices. For clarity, the finite volume method is presented for the linear convection equation:

$$\frac{\partial \boldsymbol{U}}{\partial t}+\nabla\cdot\boldsymbol{f}(\boldsymbol{U})=0 \tag{6}$$

where $\boldsymbol{f}$ is a linear vectorial function of the variable vector $\boldsymbol{U}$. Equation (6) is integrated on the elementary volumes $\Omega_{i,j,k}$ using the divergence theorem:

$$\frac{\mathrm{d}}{\mathrm{d}t}\int_{\Omega_{i,j,k}}\boldsymbol{U}\,\mathrm{d}V+\int_{\partial\Omega_{i,j,k}}\boldsymbol{f}(\boldsymbol{U})\cdot\boldsymbol{n}\,\mathrm{d}S=0 \tag{7}$$

where $\partial\Omega_{i,j,k}$ represents the faces of $\Omega_{i,j,k}$, and $\boldsymbol{n}$ is the outgoing unitary normal of $\Omega_{i,j,k}$. Supposing that $\Omega_{i,j,k}$ is an hexahedron and using the linearity of $\boldsymbol{f}$, Eq. (7) is equivalent to the relation:

$$\frac{\mathrm{d}}{\mathrm{d}t}\int_{\Omega_{i,j,k}}\boldsymbol{U}\,\mathrm{d}V+\boldsymbol{f}\left(\int_{\partial\Omega_{i,j,k}}\boldsymbol{U}\,\mathrm{d}S\right)\cdot\boldsymbol{n}=0 \tag{8}$$

Therefore, in a finite volume method, the computation of the derivatives of the convective fluxes corresponds to the calculation of the fluxes from the averaged value of $\boldsymbol{U}$ at the cell interfaces. To approximate the interface-averaged value of $\boldsymbol{U}$, an interpolation is performed using the primitive variables $\boldsymbol{W}=(u,v,w,p,T)$. In the following, the averaged value of $\boldsymbol{W}$ at the interface of the volume $\Omega_{i,j,k}$ is defined by the following:

$$\tilde{\boldsymbol{W}}=\frac{1}{|\partial\Omega_{i,j,k}|}\int_{\partial\Omega_{i,j,k}}\boldsymbol{W}\,\mathrm{d}S \tag{9}$$

and the averaged value of $\boldsymbol{W}$ in the volume $\Omega_{i,j,k}$ is defined by the following:

$$\bar{\boldsymbol{W}}=\frac{1}{|\Omega_{i,j,k}|}\int_{\Omega_{i,j,k}}\boldsymbol{W}\,\mathrm{d}V \tag{10}$$

To obtain a high-order calculation of the convective fluxes derivatives, a high-order interpolation is performed to compute the values $\tilde{\boldsymbol{W}}$. Considering the one-dimensional computational domain of Fig. 1, the interpolated vector $\tilde{\boldsymbol{W}}$ at the interface $i+1/2$ is obtained by solving the implicit relation:

$$\alpha_{i+1/2}\tilde{\boldsymbol{W}}_{i-1/2}+\tilde{\boldsymbol{W}}_{i+1/2}+\beta_{i+1/2}\tilde{\boldsymbol{W}}_{i+3/2}=\sum_{l=-1}^{2}a_l\bar{\boldsymbol{W}}_{i+l} \tag{11}$$

where $\alpha_{i+1/2}$, $\beta_{i+1/2}$, and a_l are the interpolation coefficients that are determined using a fifth-order Taylor series. The determination of these coefficients is described in detail in [11]. For a uniform Cartesian mesh, Fosso et al. [11] demonstrated that the formulation given by Eq. (11) is equivalent to Lele's sixth-order implicit compact finite difference scheme [12].

As the numerical scheme [Eq. (11)] is centered, the stability of the computations is ensured using a sixth-order selective compact filter originally introduced by Lele [12] and used by Visbal and Gaitonde [13]. The filter is applied to the flow variables at the end of each iteration to remove grid-to-grid oscillations. This filter also plays the role of an implicit subgrid-scale model for LES, relaxing turbulent energy at high frequencies [14–16]. The filtering operator applies to cell-averaged values, and it allows the filtered values denoted $\hat{\boldsymbol{W}}$ to be estimated from the unfiltered cell-averaged quantities $\bar{\boldsymbol{W}}$ in the following way:

$$\alpha_f\hat{\boldsymbol{W}}_{i-1}+\hat{\boldsymbol{W}}_i+\alpha_f\hat{\boldsymbol{W}}_{i+1}=\sum_{l=-3}^{3}\beta_l\bar{\boldsymbol{W}}_{i+l} \tag{12}$$

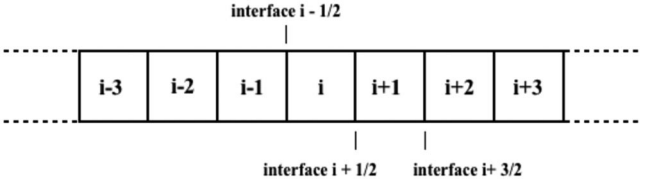

Fig. 1 Representation of a one-dimensional computational domain.

where α_f is a constant equal to 0.47, and β_l are the filter coefficients [13]. These coefficients are determined by using Taylor series and imposing that the filter transfer function is equal to zero for normalized wave number $k\Delta = \pi$, as described in [13].

The diffusive fluxes in Eq. (4) are computed using a second-order method [17]. In this method, the gradient of the primitive variables $\nabla \boldsymbol{W}$ is evaluated at the cell interfaces to compute the deformation stress $S_{i,j}$ and the heat flux vector $\boldsymbol{\Phi}$. Time discretization is performed using a low-storage six-stage Runge–Kutta algorithm [18]. Radiation boundary conditions and Navier–Stokes characteristic boundary conditions are implemented [19]. A full description of the numerical algorithm is available in the work of Fosso et al. [20].

3. *Boundary Condition for Simulation with Boundary-Layer Resolution at the Wall*

Close to the walls, the high-order schemes [Eqs. (11) and (12)] cannot be applied because of the reduced number of points available. More precisely, the variable vector at interfaces $1/2$ and $3/2$, represented by triangles in Fig. 2, cannot be computed using the four-point stencil spatial scheme [Eq. (11)]. In the same way, the selective filter cannot be applied at the points symbolized by squares. Therefore, a specific discretization must be proposed close to the boundaries. Such near-wall discretizations have been studied for finite difference schemes [21,22]. However, to the best of our knowledge, no formulation is available for a finite volume approach. Therefore, a new boundary discretization is presented here.

a. Spatial Scheme. For a wall, the boundary conditions depend on the nature of the wall and on the flow variables. The velocity satisfies a Dirichlet condition at the wall, leading to a nil velocity. The pressure follows a Neumann condition, yielding a zero wall-normal pressure gradient. The temperature satisfies a Neumann condition in the case of an adiabatic wall but a Dirichlet condition for an isothermal wall.

In this study, the implicit centered scheme on four points [Eq. (11)] is applied down to the wall. For this purpose, the computational domain is extended using ghost cells, as illustrated in Fig. 3a. In particular, a ghost interface $\boldsymbol{I}_{-1/2}$ (depicted by the dashed line) and two ghost cells (numbered P_0 and P_{-1}) are introduced. They are positioned symmetrically with respect to the wall, the locations of the points P_1 and P_2, and the interface $\boldsymbol{I}_{3/2}$.

The primitive variables (u, v, w, p, T) are reconstructed in the ghost cells to prescribe an adiabatic or an isothermal condition at the wall. More precisely, to impose a nil velocity at the wall, the velocity components are considered as odd functions along the wall-normal direction. They are computed from the values of the velocity at the points P_1 and P_2 and at the interface $3/2$, yielding the following relations:

$$\begin{cases} \bar{u}_i = -\bar{u}_{1-i} \\ \bar{v}_i = -\bar{v}_{1-i} \\ \bar{w}_i = -\bar{w}_{1-i} \end{cases} \quad \text{for } i = 0, -1, \text{ and } -1/2 \tag{13}$$

In the case of an isothermal wall, the values at the ghost points for the temperature are defined in order to specify the wall temperature T_w:

$$\bar{T}_i = 2T_w - \bar{T}_{1-i} \quad \text{for } i = 0, -1, \text{ and } -1/2 \tag{14}$$

Finally, the temperature for an adiabatic wall and the pressure are characterized by a zero gradient in the wall-normal direction. A simple way to impose this condition is to consider the temperature and the pressure as even functions with respect to the wall-normal direction. Therefore, the temperature in the ghost cells is defined by

$$\bar{T}_i = \bar{T}_{1-i} \quad \text{for } i = 0, -1, \text{ and } -1/2 \tag{15}$$

and the pressure is defined by

$$\bar{p}_i = \bar{p}_{1-i} \quad \text{for } i = 0, -1, \text{ and } -1/2 \tag{16}$$

b. Selective Filtering. The implicit centered filter on seven points [Eq. (12)] is applied down to the wall. Therefore, a third ghost cell is used, as illustrated in Fig. 3b where the additional cell is denoted by P_{-2}. A technique, similar to that previously developed for the spatial scheme, is employed to specify the flow variables in this cell, using point P_3.

In addition, to apply the implicit filter [Eq. (12)] at point P_1, filtered values at point P_0 are specified from the filtered quantities at point P_1. For instance, the velocity components are defined as follows:

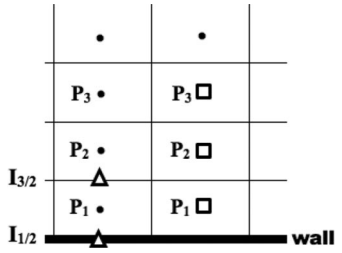

Fig. 2 Representation of interfaces (triangles (Δ)) and points (squares (□)) for which the spatial scheme and selective filter cannot be applied.

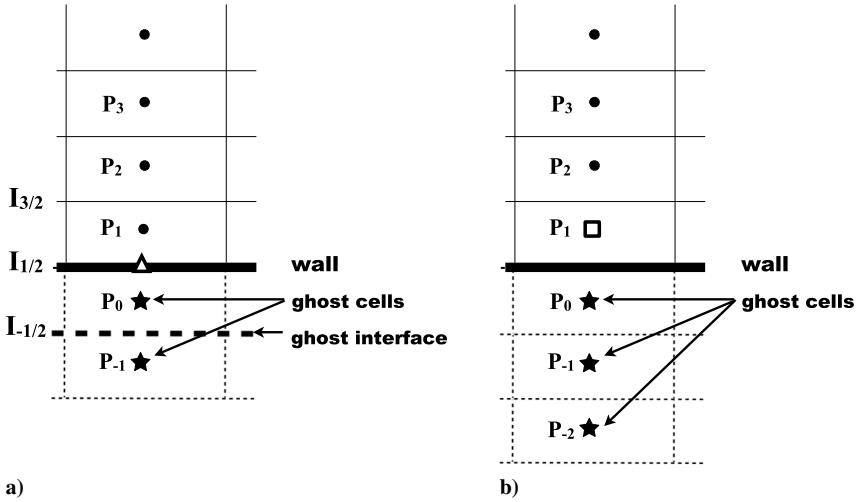

Fig. 3 Spatial discretization for a wall-resolved LES: a) for the spatial scheme [11], and b) for the selective filter [13].

$$\begin{cases} \hat{u}_0 = -\hat{u}_1 \\ \hat{v}_0 = -\hat{v}_1 \\ \hat{w}_0 = -\hat{w}_1 \end{cases} \tag{17}$$

The performance of the numerical algorithm is now evaluated for a turbulent channel flow.

B. Turbulent Channel Flow

1. Parameters

A three-dimensional turbulent channel flow is computed by LES using the wall discretization described previously. The flow is characterized by a Mach number of $M = U_b/c = 0.2$ and a friction Reynolds number of $Re_\tau = u_\tau h/\nu_w \simeq 395$, where c is the sound speed, u_τ is the friction velocity at the wall, h is the channel half-height, ν_w is the kinematic molecular viscosity at the wall, and U_b is the bulk velocity defined from the streamwise velocity u and the density ρ as follows:

$$U_b = \frac{\int_0^h \bar{\bar{\rho}}(y)\bar{\bar{u}}(y)\,\mathrm{d}y}{\int_0^h \bar{\bar{\rho}}(y)\,\mathrm{d}y} = \frac{(1/h)\int_0^h \bar{\bar{\rho}}(y)\bar{\bar{u}}(y)\,\mathrm{d}y}{\rho_b} \tag{18}$$

where ρ_b is the bulk density, and $\bar{\bar{\cdot}}$ represents a statistical mean in the homogeneous flow directions x and z. In the following, the streamwise, the wall-normal, and the spanwise spatial coordinates are denoted by x, y, and z.

Channel flows at $Re_\tau = 395$ have also been simulated by Abe et al. [23,24] and Moser et al. [25], using direct numerical simulation. In this study, the channel lengths are equal to $L_x = 2\pi h$, $L_y = 2h$, and $L_z = \pi h$, as in the DNS of Abe et al. [23]. At the top and the bottom channel walls, adiabatic conditions are imposed. Periodic conditions are applied in the streamwise and spanwise directions. To compensate the effects of the viscous dissipation, and thus impose the mass flow rate $\rho_b U_b$ in the channel, a source term S_x in the form of a pressure gradient is introduced in the streamwise momentum equation [26]. The source term is defined by the following:

$$S_x = \frac{\tau_{w_{\mathrm{ref}}}}{h} + \rho_b U_b - \frac{1}{V}\iiint_\Omega \rho u\,\mathrm{d}V \tag{19}$$

where ρ and u are instantaneous LES data, Ω is the computational domain, V represents its volume, and $\tau_{w_{\mathrm{ref}}}$ is the value of the wall shear stress of the DNS of Abe et al. [23]. A resultant term uS_x is also added in the energy equation.

2. Grid Definition

The grid parameters in the present LES including the numbers of mesh points n_x, n_y, and n_z in each direction, as well as the streamwise, normal, and spanwise grid spacings Δx^+, Δy^+, and Δz^+ in wall units, are given in Table 1. At the wall, the grid spacing Δy_w^+ is equal to one in order to capture the small structures developing in the near-wall regions. From the wall, the mesh is stretched in the y direction to reach $\Delta y_{\max}^+ = 8$ at the center of the channel in order to reduce computational cost. The stretching rate remains lower than 4% to avoid the generation of spurious numerical waves. In the streamwise and the spanwise directions, the grid spacings are uniform, and they are equal to $\Delta x^+ = 15$ and $\Delta z^+ = 10$. For comparison, the grid parameters used in the DNS of Abe et al. [23] and Moser et al. [25] are also provided in Table 1. The DNS grids are finer than the LES mesh, particularly in the wall-normal direction where the mesh spacing Δy_w^+ is close to 0.2; whereas $\Delta y_w^+ = 1$ in the LES.

Table 1 Grid parameters to simulate a turbulent channel flow at $Re_\tau = 395$

Simulation	$n_x \times n_y \times n_z$	Δx^+	Δz^+	Δy_w^+	$\Delta y_{\max}^+$
LES	$161 \times 181 \times 241$	15	5	1	8
DNS [23]	$256 \times 192 \times 256$	10	5	0.2	9.6
DNS [25]	$256 \times 193 \times 192$	10	6.5	0.15	6.5

3. Initial Conditions

At initial time $t = 0$, the streamwise velocity u in the channel is given by the analytical turbulent profile:

$$u(y) = \frac{8}{7}U_b\left(\frac{y}{h}\right)^{1/2} \tag{20}$$

and the velocity components in directions y and z are equal to zero. Initially, the static pressure p_0 and the static temperature T_0 are uniform, with $p_0 = 10^5$ Pa and $T_0 = 273$ K. The transition toward turbulence is accelerated by adding perturbations in the form of spanwise vortices to the initial velocity profile [27]. The time step Δt for the simulation is chosen so that the Courant–Friedrichs–Lewy number is $\mathrm{CFL} = c\Delta t/\Delta y_w \simeq 0.7$ to ensure the stability of time integration. The transient period of the simulation lasts during the nondimensional time $t^* = tU_b/h = 102$, which is equivalent to 15 flow periods through the channel. The statistics are then collected during a time period of $t^*_{\mathrm{stat}} \simeq 100$. The results are averaged in time and in space in the homogeneous directions x and z, and they are compared with the DNS data [23,24].

4. Results

The mean and rms values of the streamwise velocity $u^+ = <u>/u_\tau$ and $u'^+ = <u'u'>^{1/2}/u_\tau$ obtained in the LES are represented by the dashed lines in Fig. 4, where $<\cdot>$ corresponds to a statistical mean in time and space in the homogeneous flow directions. The results are displayed in wall units as a function of the radial distance y^+, and they are compared with the DNS data of Abe et al. [24]. A good agreement between the LES and DNS profiles is found for both mean and rms quantities. This suggests that the present numerical algorithm, based on the application of a selective filter as a subgrid-scale model for LES, can be used to simulate turbulent wall-bounded flows at low Reynolds numbers. Note that the influence of the spatial resolution of the channel on the LES results is discussed in the Appendix.

III. Simulations Using a Wall Model

A. Numerical Approach

1. Description of the Wall Model

When flows at high Reynolds numbers are considered, a wall modeling must be introduced. The wall model [9] used here relies on Reichardt's [28] and Kader's [29] analytical laws. The first one allows the mean velocity U to be estimated as a function of the height y above the wall. In wall units, one gets

$$u^+ = \frac{U}{\sqrt{\tau_w/\rho_w}} = \frac{1}{\kappa}\ell_n(1+\kappa y^+) + \left(B - \frac{1}{\kappa}\ell_n\,\kappa\right)\left(1 - \exp\left(-\frac{y^+}{11}\right) - \frac{y^+}{11}\exp(-0.33y^+)\right) \tag{21}$$

where $y^+ = \rho_w u_\tau y/\mu_w$, μ_w is the dynamic molecular viscosity at the wall, κ is the von Kármán constant equal to 0.41, and B is a constant equal to 5.25. The Kader law approximates the variations of the temperature T as, in wall units,

$$T^+ = -\frac{(T - T_w)\rho_w C_p u_\tau}{\Phi_w} = Pry^+\exp(\Gamma) + \left(2.12\ln(1+y^+) + (3.85Pr^{1/3} - 1.3)^2 + 2.12\ln Pr\right)\exp\left(\frac{1}{\Gamma}\right) \tag{22}$$

where

$$\Gamma = -(10^{-2}(Pry^+)^4)/(1 + 5Pr^3y^+)$$

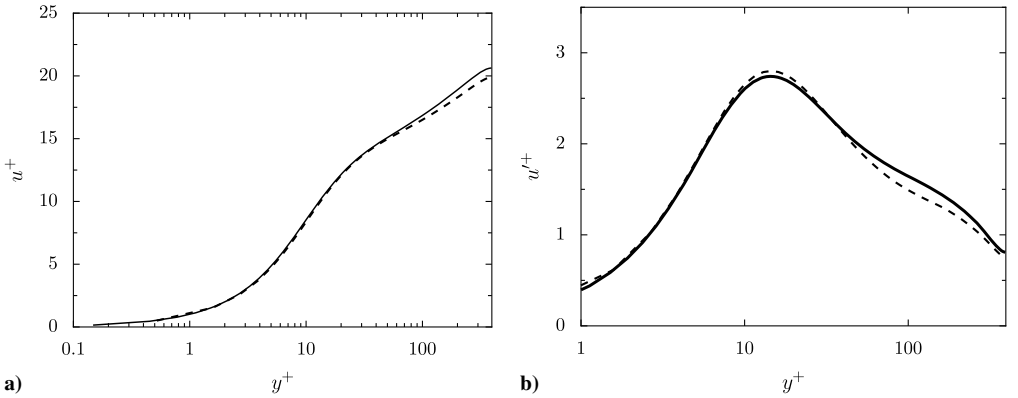

Fig. 4 Streamwise velocity profiles in the channel: a) mean, and b) rms. Dashed lines denote LES, and solid lines denote DNS of [24].

In addition, in the boundary layer, the pressure variations are assumed to be negligible in the wall-normal direction, yielding

$$\frac{\partial p}{\partial y} = 0 \tag{23}$$

Equations (21) and (22) are valid for incompressible flows, assuming weak pressure gradients in the streamwise direction. The validity of these wall laws can be extended to compressible flows thanks to van Driest's transformation [30].

When a wall model is used to compute a wall-bounded flow, the inner part of the boundary layer close to the wall is simulated without resolving the turbulent structures developing in this region. As a consequence, a coarse mesh can be used near the wall and the computational cost is considerably reduced compared to a wall-resolved simulation. In our finite volume approach, the wall model is involved in the computation of the variable vector $\boldsymbol{W}$ and its gradient $\nabla \boldsymbol{W}$ at the wall. Indeed, the value of $\nabla \boldsymbol{W}$ at the wall cannot be obtained in the same way as for a wall-resolved LES. In particular, the velocity and the temperature gradients at the wall are not correctly predicted by the numerical schemes. Consequently, the wall model allows the velocity and the temperature gradients to be estimated at each temporal iteration. In practice, the model gives estimations of the wall shear stress $\tau_w = \mu_w \partial U/\partial y|_{y=0}$ and of the wall heat flux $\Phi_w = -\lambda \partial T/\partial y|_{y=0}$, as illustrated in Fig. 5.

2. *Estimation of Velocity and Temperature Gradients at the Wall*

To obtain the values of τ_w and Φ_w from Reichardt's [28] and Kader's [29] laws, the values of the velocity U and the temperature T that appear in Eqs. (21) and (22) need to be determined. For that, a computational point M located at a distance y_M from the wall is chosen. This point M is named the matching point [7]. Represented in Fig. 5, it is the center of one of the cells located along the wall-normal direction. It must be located in the inner part of the boundary layer such that the conditions of application of the wall laws are satisfied. The choice of the position of the matching point will be discussed in Sec. III.A.4. To compute the values of U and T, the instantaneous LES variables at point M are collected. They are denoted $\boldsymbol{u}_{\text{LES}}$ and T_{LES} in Fig. 5. The scalar velocity value U is obtained by writing the velocity vector $\boldsymbol{u}_{\text{LES}}$ in the local coordinate frame defined by the flow direction $\boldsymbol{m}$, the wall-normal direction $\boldsymbol{n}$, and the vector $\boldsymbol{m} \wedge \boldsymbol{n}$. The components of $\boldsymbol{u}_{\text{LES}}$ in this frame are denoted u_m, u_n, and $u_{m\wedge n}$; and the velocity U is given by the relation $U = \sqrt{u_m^2 + u_{m\wedge n}^2}$. The temperature T is equal to T_{LES}. To determine the values of τ_w and Φ_w from relations (21) and (22), it is also necessary to estimate the values of the temperature T_w, the dynamic viscosity μ_w, and the density at the wall ρ_w. These quantities are computed differently, depending on the isothermal or the adiabatic nature of the wall.

a. Isothermal Wall. In the case of an isothermal wall, the temperature at the wall T_w is known. Therefore, the dynamic viscosity at the wall μ_w is computed from Sutherland's law for the temperature T_w. Then, the wall density ρ_w is obtained using the perfect gas equation, yielding $\rho_w = p_{\text{LES}}/(RT_w)$, where p_{LES} is the value of the pressure from the LES field at point M and R is the perfect gas constant. From the quantities T_w, μ_w, ρ_w, U, and T, the wall laws can now be used to estimate the velocity and the temperature gradients at the wall. The friction velocity u_τ is estimated from Reichardt's law [28] using a Newton algorithm. The wall shear stress $\tau_w = \rho_w u_\tau^2$ is then computed. As for the wall heat flux Φ_w, it is obtained from Kader's law [29] and $T = T_{\text{LES}}$.

b. Adiabatic Wall. In the case of an adiabatic wall, the value of Φ_w is equal to zero, leading to $T_w = T_{\text{LES}}$. The wall shear stress τ_w is then computed in the same way as for an isothermal wall.

3. *Implementation with High-Order Numerical Schemes*

As for the wall-resolved LES approach, the high-order schemes [Eqs. (11) and (12)] cannot be applied down to the wall. Consequently, in this study, for the LES with wall modeling, new spatial discretizations for the spatial scheme [Eq. (11)] and the selective filter [Eq. (12)] have been proposed in the near-wall regions. More precisely, the velocity components u, v, and w; the pressure p; and the temperature T at the cells and interfaces represented by symbols in Fig. 2 are computed differently from the interior points. The wall model is involved in this procedure.

a. Spatial Scheme. The wall discretization depends on the variables and the adiabatic or the isothermal nature of the wall. A first discretization is proposed for the variables satisfying a Dirichlet

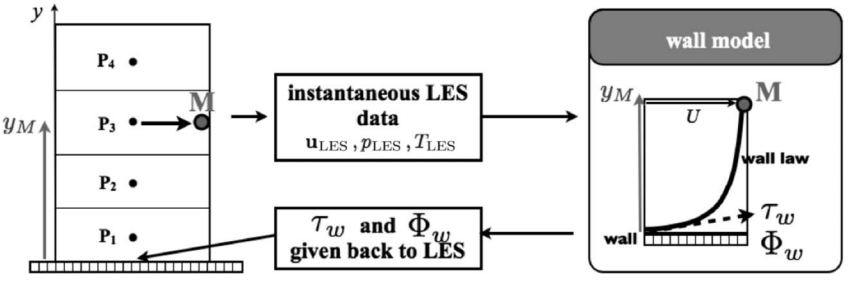

Fig. 5 Wall model application. The values of τ_w and Φ_w are computed by the model using instantaneous LES data at matching point M.

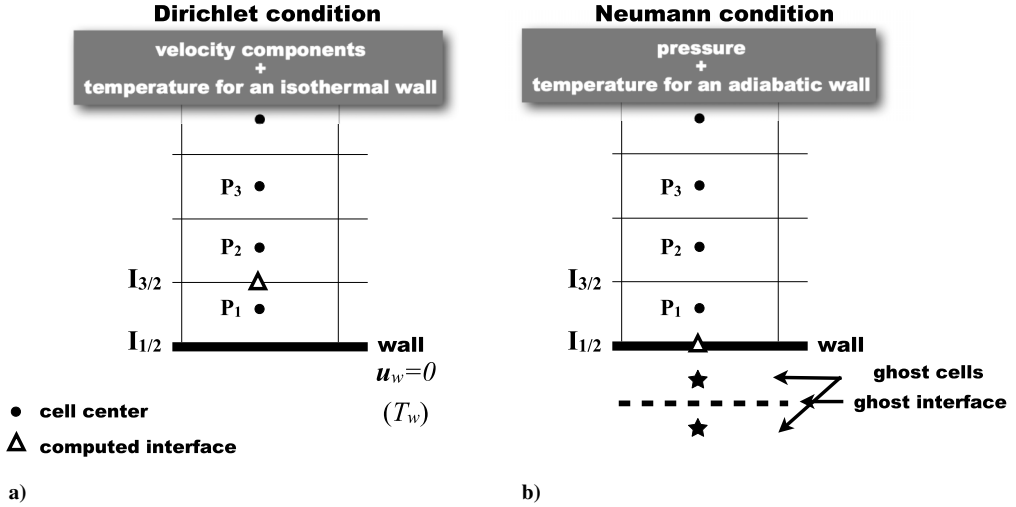

Fig. 6 Spatial discretization close to the wall for the spatial scheme [11] in the case of a wall-modeled LES: a) Dirichlet condition, and b) Neumann condition at the wall.

condition, such as the velocity components and the temperature for an isothermal wall. A second discretization is used for the variables verifying a Neumann condition such as the pressure and the temperature in the case of an adiabatic wall. For clarity, the discretizations corresponding to the Dirichlet and the Neumann conditions are presented for the velocity and the pressure, respectively.

For a Dirichlet condition, the no-slip condition $\boldsymbol{u}_w = \boldsymbol{0}$ is imposed at the wall, as illustrated in Fig. 6a. The velocity vector $\tilde{\boldsymbol{u}}_{3/2}$, at the interface between points P_1 and P_2, is computed using a second-order centered scheme:

$$\tilde{\boldsymbol{u}}_{3/2} = \alpha''_{3/2}\bar{\boldsymbol{u}}_1 + \beta''_{3/2}\bar{\boldsymbol{u}}_2 \tag{24}$$

where $\alpha''_{3/2}$ and $\beta''_{3/2}$ are the interpolation coefficients, determined using the second-order Taylor series.

In the case of a Neumann condition, the spatial discretization is similar to the one used in the wall-resolved LES approach and described in Sec. II.3. To apply the four-point implicit centered scheme [Eq. (11)] down to the wall, two ghost cells and a ghost interface are introduced, as represented in Fig. 6b. The values of the pressure in these cells are computed to impose $\partial p/\partial y|_{y=0} = 0$ using relation (16).

b. Selective Filtering. The selective filter is applied down to the wall, using three rows of ghost cells. The definition of the ghost cells depends on the Neumann or the Dirichlet conditions satisfied by the flow variables at the wall.

For a Neumann condition, three ghost cells are introduced beyond the wall. They are represented in Fig. 7b and reconstructed in the same way as for the spatial scheme [11].

For the variables satisfying a Dirichlet condition at the wall, such as the velocity, three new cells are added between the wall and the point P_1. These cells allow us to apply the filter down point P_1. They are symbolized by stars in Fig. 7a. The methodology used to define the velocity in these cells is now presented. In the following, these cells correspond to points P_0, P_{-1}, and P_{-2}. Their positions from the wall are defined by $y_i = h_1/d_i$, where h_1 is the height of the point P_1; i is the index of point P_i; and d_0, d_1, and d_2 are constants chosen such as $d_0 < d_{-1} < d_{-2}$. The importance of the ghost cell locations, determined by the values of d_i, is discussed in Sec. III.B.2. To specify the velocity in these additional cells, the wall model is used. The wall shear stress τ_w is determined from Reichardt's law [28] and the LES data collected at the matching point M, as described in the previous section. Once the value of τ_w obtained, the Reichardt law provides a relation for the mean velocity U as a function of the wall distance y, as plotted in Fig. 7a. This wall law profile is then used to compute the mean velocity U_i for $i = 0$, -1, and -2. A similar reconstruction allows the temperature to be specified using Kader's law [29]. The velocity vectors in the ghost cells are then computed from the values of U_i. They are assumed to be colinear with the velocity $\boldsymbol{u}_1$ at point P_1:

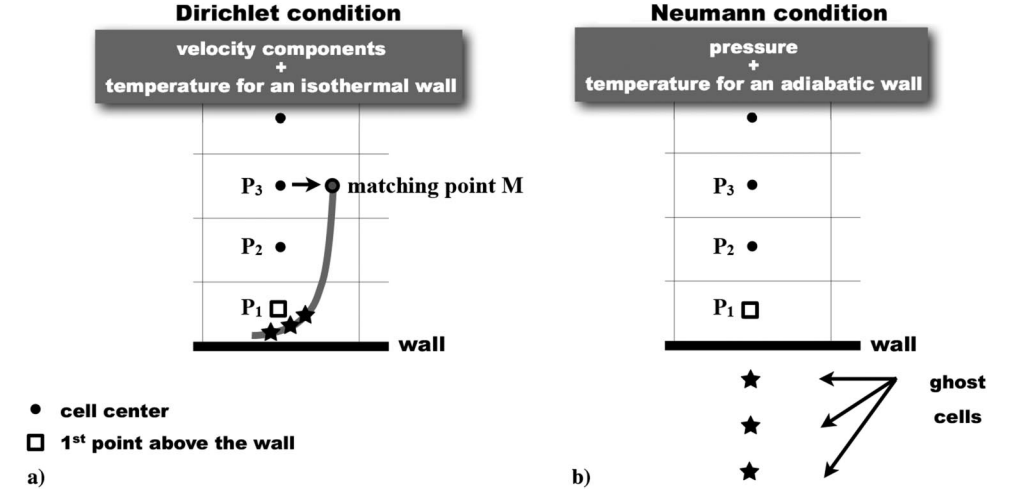

Fig. 7 Spatial discretization close to the wall for the selective filter [13] in the case of a wall-modeled LES: a) Dirichlet condition, and b) Neumann condition at the wall.

$$\boldsymbol{u}_i = U_i \frac{\boldsymbol{u}_1}{\|\boldsymbol{u}_1\|} \tag{25}$$

Finally, in order to apply the implicit centered filter [Eq. (12)] at point P_1, the filtered velocity $\hat{\boldsymbol{u}}_0$ at point P_0 is needed. The filter is assumed to have no effect on the velocity field at point P_0, leading to the approximation $\hat{\boldsymbol{u}}_0 = \bar{\boldsymbol{u}}_0$.

4. *Influence of the Matching Point Location*

The matching point M, represented in Figs. 5 and 7a, plays a considerable role in the wall-modeled LES approach, as it provides the LES data used to estimate the values of τ_w and Φ_w. Therefore, the influence of its position must be examined. Usually [9], this point corresponds to first computational point P_1 above the wall. However, recent works [7,31] demonstrated that selecting a matching point located further from the wall improves results. Two reasons for that can be raised. First, the smallest structures captured by a mesh are necessarily under-resolved near the mesh cutoff scale. Because these small structures have a major influence on the development of the flow in the near-wall region, the LES flowfield is not accurately computed at the first points above the wall. Second, as presented previously, the high-order discretization must generally be adapted when approaching the wall, which may produce numerical errors in this region. The influence of the choice of the matching point location on the LES results will be investigated in the following section, where the performance of the numerical approach with wall modeling is examined for a turbulent channel flow.

B. Turbulent Channel Flows

1. *Parameters*

The LES approach with wall modeling is used to compute the turbulent channel flow at a Mach number of $M = 0.2$ and a friction Reynolds number of $Re_\tau \simeq 2000$, which was also considered by Hoyas and Jiménez [32] using DNS. The channel lengths are equal to $L_x = 2\pi h$, $L_y = 2h$, and $L_z = \pi h$, as in the LES of the previous section for the channel flow at $Re_\tau = 395$. Periodic conditions are implemented in directions x and z. At the walls, adiabatic or isothermal boundary conditions are specified. The mass flow rate $\rho_b U_b$ in the channel is imposed using the source term S_x defined in Eq. (19) and its resultant term uS_x. In the case of an isothermal wall, the wall temperature T_w is imposed and an additional source term Q_x is introduced [26] in the energy equation to prescribe the bulk temperature T_b. The temperature T_b is obtained from the averaged values of ρ, u, and T in the homogeneous directions x and z using the following relation:

$$T_b = \frac{\int_0^h \bar{\bar{\rho}}(y)\bar{\bar{u}}(y)\bar{\bar{T}}(y)\,\mathrm{d}y}{\int_0^h \bar{\bar{\rho}}(y)\bar{\bar{u}}(y)\,\mathrm{d}y} \tag{26}$$

and the source term Q_x is defined by

$$Q_x = -\frac{\Phi_{w_{\text{ref}}}}{h} + T_b - \frac{1/V \iiint_\Omega \rho u T\,\mathrm{d}V}{1/V \iiint_\Omega \rho u\,\mathrm{d}V} \tag{27}$$

where ρ, u, and T are instantaneous LES data; and $\Phi_{w_{\text{ref}}}$ is a wall heat flux estimated from the empirical correlation of Sleicher and Rouse [33] in order to impose a temperature gradient at the wall corresponding to $T_b/T_w = 1.1$.

At initial time $t = 0$, the streamwise velocity u in the channel is identical to that of the LES of the turbulent channel flow at $Re_\tau = 395$. The velocity components in directions y and z are equal to zero. The static pressure and temperature are equal to $p_0 = 10^5$ Pa and $T_0 = 293$ K. The time step is chosen such that $\mathrm{CFL} = c\Delta t/\Delta y \simeq 0.7$. The simulation transient period lasts during the nondimensional time $t^* = tU_b/h = 200$, corresponding to 30 flow periods through the channel. Then, the statistics are sampled over 30 flow periods. The results are averaged in time and in space, and they are compared with the results of the DNS of Hoyas and Jiménez [32]. In the case of isothermal walls, the temperature profile is compared with the profile given by the analytical law of Kader [29].

2. *Results for Adiabatic Walls*

a. Choice of the Matching Point Location. The influence of the matching point on the LES results is evaluated by performing four simulations using matching points located at different positions y_M^+ from the wall. These positions are those of cell centers P_1, P_2, P_3, or P_4. The mesh used for the computations is designed to satisfy the grid constraints for LES with wall modeling proposed by Bocquet et al. [9]. In particular, the grid cells are chosen to capture the large turbulent structures of the outer region of the boundary layers. These structures, elongated in the streamwise direction, are found for $y^+ > 100$. Therefore, the grid spacing of the mesh in the wall-normal direction is equal to 100 in wall units. In the streamwise and spanwise directions, the mesh spacings in wall units are, respectively, equal to 200 and 100. In that way, matching points P_1, P_2, P_3, and P_4 are, respectively, located at $y_M^+ = 50$, 150, 250, and 350 in wall units. In the computation, the ghost cell positions are arbitrarily chosen using $d_0 = 1.3$, $d_{-1} = 1.5$, and $d_{-2} = 2$, according to the notations introduced in Sec. III.A.3.

The profiles obtained for the mean and rms streamwise velocities and for the Reynolds shear stresses $-<uv'>/u_\tau$ are displayed in Fig. 8. They are plotted in wall units as a function of the wall distance y^+, and they are compared with DNS profiles [32]. The matching points are indicated by symbols. They are all located on the DNS mean velocity profile in Fig. 8a, which supports that the numerical algorithm with wall modeling is correctly implemented. For the LES performed with the matching point P_1 closest to the wall, the mean and rms profiles present discrepancies with respect to the DNS profiles. In particular, the amplitude of the mean velocity and those of the Reynolds stresses are underpredicted over all the channel half-height. On the contrary, the use of matching point P_2 leads to an overprediction of the mean velocity u^+ in the logarithmic region with respect to the DNS results. However, turbulent levels in better agreement with the DNS data are obtained as compared to the LES

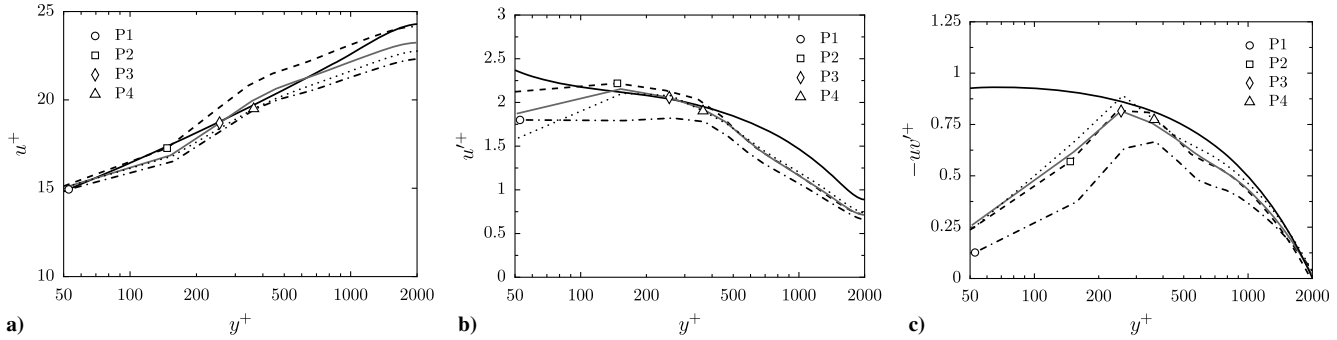

Fig. 8 Representations of a) mean streamwise velocities, b) rms streamwise velocities, and c) Reynolds shear stresses: LESs using P_1 (dashed–dotted lines), P_2 (dashed lines), P_3 (grey, solid lines) and P_4 (dotted lines); DNS of [32] (black, solid lines).

results determined using P_1. Finally, the best match with the DNS data for both the mean and rms profiles is observed for the LES using matching points P_3 and P_4. These results demonstrate the importance of choosing a matching point located far from the wall, for $y^+ > 150$, to predict the turbulent intensities in the channel with a good accuracy. Therefore, in the following, point P_3 is selected as the matching point in the computations.

b. Influence of the Position of the Ghost Cells. In Sec. III.A.3, ghost cells have been introduced for LES with wall modeling in order to apply the selective filter towards the wall. The influence of the position of these cells on the LES results is evaluated by performing four simulations (G1, G2, G3, and G4) using different ghost cell locations. The ghost cell configuration for each LES is illustrated in Fig. 9. In LES G1, the ghost cells are regularly distributed between the wall and point P_1. In LESs G2, G3, and G4, these cells are located between $y = 0.5y_{P_1}$ and point P_1. More precisely, for LES G2, the ghost cells are located at $0.5y_{P_1}$, $2y_{P_1}/3$, and $5y_{P_1}/6$. In LES G3, the ghost cell positions are arbitrarily chosen as $0.5y_{P_1}$, $2y_{P_1}/3$, and $y_{P_1}/1.3$. This configuration was used in the previous section dealing with the effects of the matching point location. Finally, in LES G4, the ghost cells are positioned at $y = 0.5y_{P_1}$, $5y_{P_1}/8$, and $0.75y_{P_1}$. The mesh used in the four LESs is identical to that in the study reported previously. Moreover, the matching point is point P_3.

The mean velocity profiles u^+ obtained in LESs G1, G2, G3, and G4, as well as in the DNS of Hoyas and Jiménez [32], are depicted in wall units in Fig. 10a as a function of the wall distance. The four LES profiles are superimposed, which suggests that the choice of the ghost cell positions, between the wall and point P_1, has a weak influence on the mean velocity in the channel. They are also in good agreement with the DNS profile, except in the wake region where the velocity is slightly underestimated.

The fluctuating velocity profiles u'^+ and Reynolds stresses $-uv'^+$ from the LES and from the DNS of Hoyas and Jiménez [32] are displayed in Figs. 10b and 10c in wall units. The LES profiles have similar shapes. Compared to the DNS data, the turbulence intensities from the LES are lower. The highest turbulent levels are observed in LESs G3 and G4. The best agreement with the DNS results is obtained in LES G3.

These results demonstrate that the choice of the ghost cell positions does not considerably affect the LES results. In the following, the ghost cell positions defined for the LES G3 are used.

c. Study of the Grid Sensitivity. The influence of the spatial resolution is investigated by performing wall-modeled LES (WMLES) on meshes with different grid spacings. The mesh parameters, including the numbers of points n_x, n_y, and n_z in each direction; the grid spacings Δ^+, and the matching point location $y^+_{P_3}$ (in wall units), as well as the grid spacing $\Delta x/h$ normalized by the channel half-height, are provided in Table 2. In all directions, the grid spacing is uniform. To examine the influence of the mesh spacing in directions x, y, and z, three groups of meshes named grid$x$, grid$y$ and grid$z$ are considered. For grid$x$300, grid$x$200, and grid$x$100, the mesh spacings Δz^+ and Δy^+ are equal to 100; whereas Δx^+ reduces from 300 to 100. In grid$y$150, grid$y$100, and grid$y$50, $\Delta x^+ = 200$ and $\Delta z^+ = 100$ are imposed; whereas Δy^+ decreases from 150 down to 50. Finally, in grid$z$150, grid$z$100, and grid$z$50, $\Delta x^+ = 200$; $\Delta y^+ = 100$; and $\Delta z^+ = 150$, 100, and 50 are specified. Note that the position of the matching point is $y^+_{P_3} = 250$ in all the LESs using grid$x$ and grid$z$ meshes, but it varies from $y^+_{P_3} = 125$ to $y^+_{P_3} = 375$ using grid$y$ meshes.

For comparison, the characteristics of the mesh in the DNS of Hoyas and Jiménez [32], as well as those of the grids used to perform wall-modeled LES in the literature [9,34–36], are reported in Table 2. Compared to the DNS mesh, grid$x$200 is 25 times coarser in directions x and z, and it is 330 times coarser in direction y at the wall. Furthermore, note that the grid parameters chosen in this study are close to those used in the wall-modeled LES of the literature.

In the following, the influence of the mesh resolution is examined by representing the profiles of the mean streamwise velocity u^+, the rms streamwise velocity u'^+, and the Reynolds shear stresses $-uv'^+$ as functions of the wall distance y^+ in wall units. The maching points (MP) are indicated by symbols in the figures. The LES profiles are compared with the profiles given by the DNS of Hoyas and Jiménez [32].

Regarding the influence of the mesh resolution in the wall-normal direction, the results obtained in simulation grid$y$ are displayed in Fig. 11. The mean velocity profiles differ in the logarithmic region, whereas they have similar shapes for $y^+ > 1000$. A better agreement

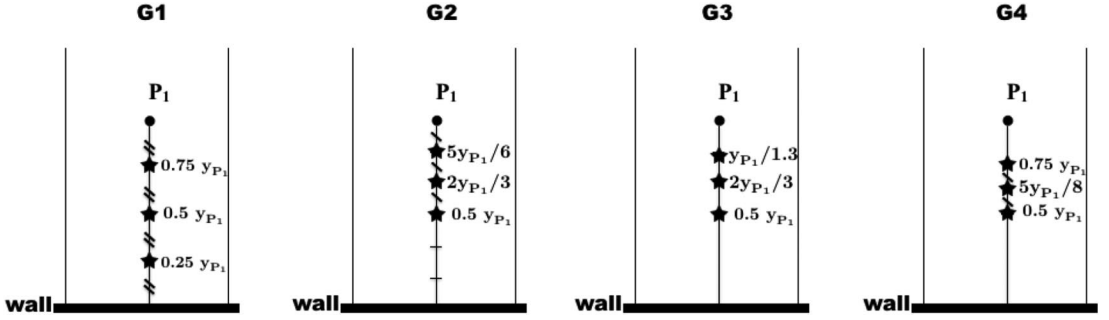

Fig. 9 Representation of the ghost cell positions (⋆) in the wall-normal direction for LESs G1, G2, G3, and G4.

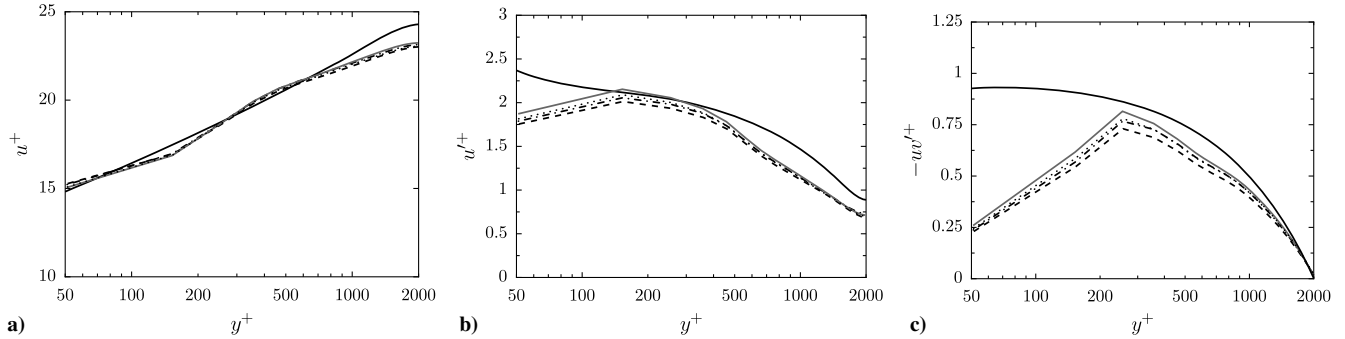

Fig. 10 Representations of a) mean streamwise velocities, b) rms streamwise velocities, and c) Reynolds shear stresses: LESs G1 (dashed–dotted lines), G2 (dashed lines), G3 (grey, solid lines), and G4 (dotted lines); DNS of [32] (black, solid lines).

Table 2 Grid parameters

Simulation	$n_x \times n_y \times n_z$	Δx^+	Δz^+	Δy_w^+	$\Delta y_{\max}^+$	Matching point $y_{P_3}^+$	$\Delta x/h$
WMLES grid$x$300	$43 \times 41 \times 65$	300	100	100	100	250	0.15
WMLES grid$x$200	$65 \times 41 \times 65$	200	100	100	100	250	0.10
WMLES grid$x$100	$127 \times 41 \times 65$	100	100	100	100	250	0.05
WMLES grid$y$150	$65 \times 27 \times 65$	200	100	150	150	375	0.10
WMLES grid$y$100	$65 \times 41 \times 65$	200	100	100	100	250	0.10
WMLES grid$y$50	$65 \times 81 \times 65$	200	100	50	50	125	0.10
WMLES grid$z$150	$65 \times 41 \times 43$	200	150	100	100	250	0.10
WMLES grid$z$100	$65 \times 41 \times 65$	200	100	100	100	250	0.10
WMLES grid$z$50	$65 \times 41 \times 127$	200	50	100	100	250	0.10
DNS of Hoyas and Jiménez [32]	$1536 \times 633 \times 1536$	8.2	4.1	0.3	8.9	— —	0.004
WMLES of Bodart and Larsson [34]	— —	200	40	125	125	300	0.10
WMLES of Bocquet et al. [9]	— —	260	160	100	100	50	0.13
WMLES of Lee et al. [35]	— —	200	135	125	125	312	0.10
WMLES of Park and Moin [36]	— —	200	125	40	40	200	0.10

with the DNS is obtained using grid$y$150 and grid$y$100 than using grid$y$50, suggesting that coarse cells must be used in the wall-normal direction. In the same way, in Fig. 11b, the rms profile from the LES using grid$y$50 presents discrepancies with the DNS result on the channel half-height with a peak at $y^+ = 75$. On the contrary, using grid$y$100 and grid$y$150, the turbulent intensities are better predicted. In particular, the matching points are located on the DNS profiles in these cases. In Fig. 11c, the LES Reynolds stresses are lower when compared to the DNS result. For $y^+ > 500$, the highest turbulent levels are obtained using grid$y$150, supporting the idea to choose $\Delta y^+ > 100$, as is generally found in the literature [9,34,35].

Regarding the influence of the mesh resolution in the spanwise direction, the profiles obtained using grid$z$150, grid$z$100, and grid$z$50 are represented in Fig. 12. The mean and rms velocity profiles are superimposed. In particular, the mean velocity is correctly estimated in the logarithmic region, but its value is underpredicted compared to the DNS profile in the wake area. The turbulent intensities u'^+ are well predicted near the matching point for $y^+ \simeq 250$, and they are underestimated for $y^+ > 500$. The Reynolds stresses profiles obtained using grid$z$150 and grid$z$100 are very similar, whereas that from the LES using grid$z$50 provides higher turbulent levels, which are in better agreement with the DNS profile for $y^+ \geq 250$.

Regarding the influence of the mesh resolution in the streamwise direction, the profiles obtained in the LES with $100 \leq \Delta x^+ \leq 300$ are plotted in Fig. 13. They are very close to those represented in Fig. 12. They are superimposed over all the channel half-height, indicating grid convergence in direction x. According to these results, $\Delta x^+ = 300$ is sufficient for wall-modeled LES, although $\Delta x^+ \leq 260$ is generally chosen in the literature [9,34,35].

3. *Results for Isothermal Walls*

For simulations with isothermal walls as described in Sec. III.B.1, unfortunately, no corresponding DNS data are available. To bypass this issue, the results of the DNS of Hoyas and Jiménez [32] for the channel flow at $Re_\tau = 2000$ with adiabatic walls are used. Indeed, the flow has a low Mach number and the temperature gradient at the wall is sufficiently weak to consider the temperature as a passive scalar. The flow regime is considered as quasi incompressible in this case.

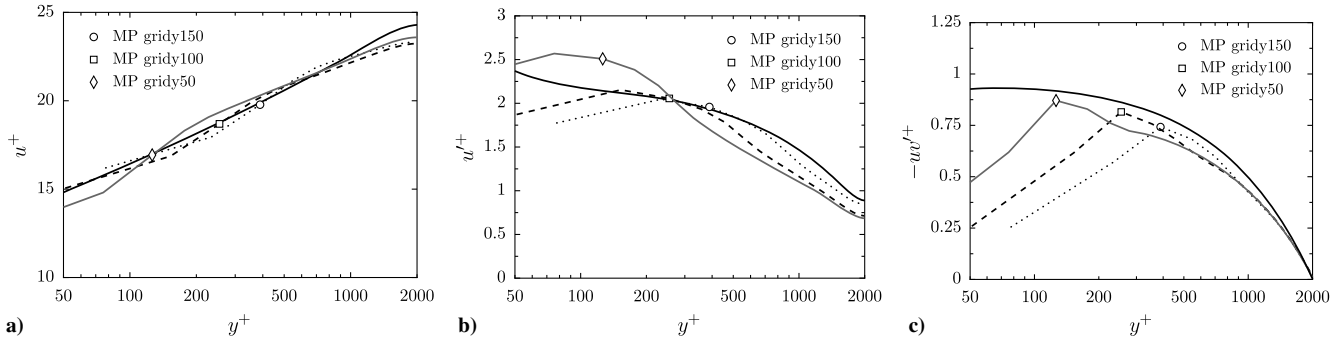

Fig. 11 Representations of a) mean streamwise velocities, b) rms streamwise velocities, and c) Reynolds shear stresses: LESs using grid$y$150 (dotted lines), grid$y$100 (dashed lines), and grid$y$50 (grey, solid lines); DNS of [32] (black, solid lines).

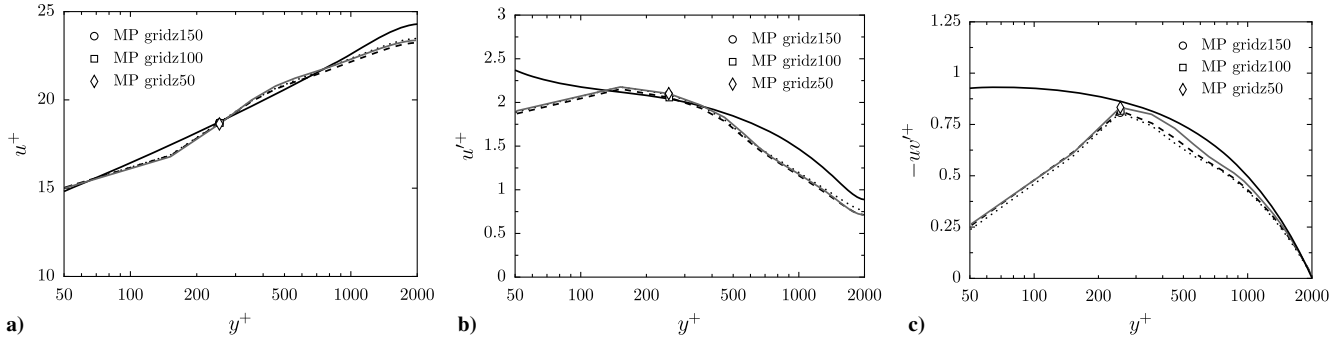

Fig. 12 Representations of a) mean streamwise velocities, b) rms streamwise velocities, and c) Reynolds shear stresses: LESs using grid$z$150 (dotted lines), grid$z$100 (dashed lines), and grid$z$50 (grey, solid lines); DNS of [32] (black, solid lines).

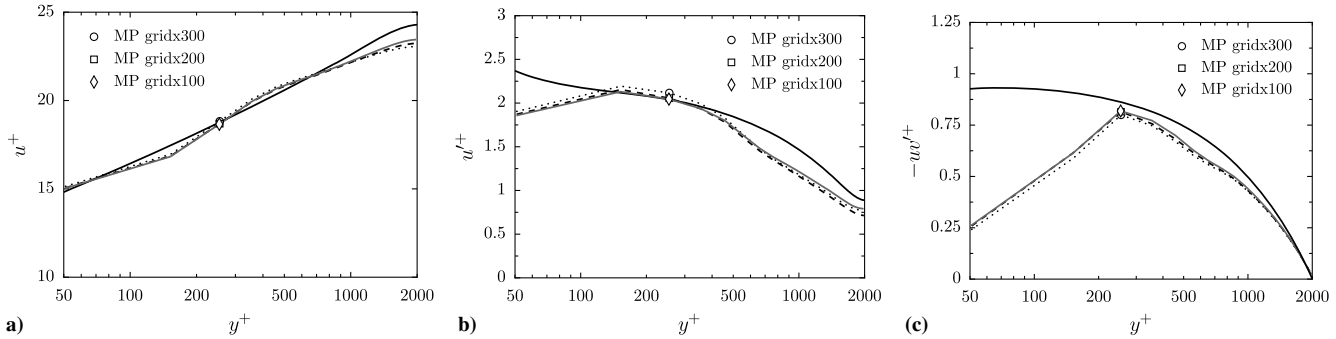

Fig. 13 Representations of a) mean streamwise velocities, b) rms streamwise velocities, and c) Reynolds shear stresses: LESs using grid$x$300 (dotted lines), grid$x$200 (dashed lines), and grid$x$100 (grey, solid lines); DNS of [32] (black, solid lines).

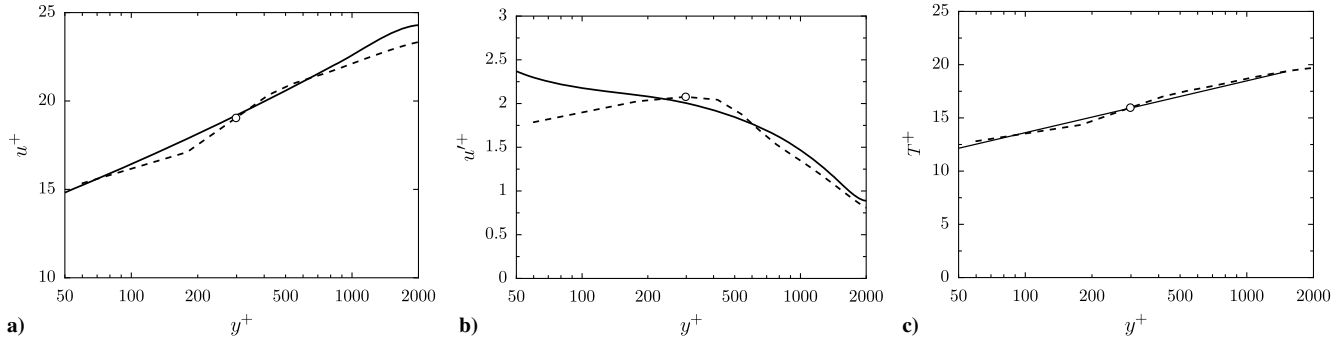

Fig. 14 Representations of a) mean and b) rms streamwise velocities: LES (dashed lines), and DNS of [32] (solid lines); and c) mean temperature: LES (dashed line) and Kader's law [29] (solid lines).

For brevity, only the results obtained using grid$x$200 are presented. The mean velocity u^+ and the rms component u'^+ are depicted in Figs. 14a and 14b, in wall units, as functions of the wall distance. They are compared with the DNS results of Hoyas and Jiménez [32]. The LES results are close to those given by the simulations with adiabatic walls in the previous section. The mean velocities obtained in the LES and in the DNS are in good agreement in the logarithmic zone, whereas small discrepancies are reported in the wake region for $y^+ > 1000$. The matching point represented by a circle in Fig. 14a is located on the DNS velocity profile. In Fig. 14b, the LES profile is close to the DNS profile for wall distances greater than the matching point position: that is, for $y_M^+ > 250$.

The evolution of the mean temperature along the wall distance y^+ is displayed in wall units in Fig. 14c. The profile estimated by Kader's law [29] is also represented for comparison. It is obtained from the wall law given by relation (22) using the values of the wall shear stress τ_w and the wall heat flux Φ_w, respectively, computed from the empirical coefficients of Petukhov [37] and Sleicher and Rouse [33]. The LES profile is in very good agreement with Kader's law [29].

These results suggest the capability of the present numerical algorithm to correctly estimate thermal effects with wall-modeled LES.

IV. Conclusions

In this paper, a numerical procedure is presented to perform a LES of wall-bounded flows using high-order implicit numerical schemes. The spatial discretization in the LES approach is carried out using a sixth-order compact scheme in conjunction with a sixth-order selective filter. A ghost cell reconstruction is proposed to apply these schemes in the near-wall regions. This approach is validated by computing a turbulent channel flow at a Reynolds number of $Re_\tau = 395$. In this case, the results agree very well with DNS data, which demonstrate that the LES algorithm, based on the use of a selective filter as a subgrid-scale model, can be applied to compute wall-bounded turbulent flows. For flows at high Reynolds numbers, a wall model is coupled with the high-order schemes to carry out LESs at an acceptable computational cost. In particular, a ghost cell reconstruction from the wall law velocity and temperature profiles is performed in order to apply the selective filter down to the wall. In addition, a matching point, for data exchange between the wall model and the LES algorithm, has to be chosen. The performance of the wall-modeled LES approach is examined for a turbulent channel flow at $Re_\tau = 2000$. The choice of the matching point is found to have a considerable influence on the LES results. Selecting a matching point far from the wall (typically for $y^+ > 150$) provides turbulent intensities in fairly good agreement with the DNS results of the literature, whereas the turbulent levels are underpredicted when the matching point is the first point above the wall. On the contrary, the choice of the ghost cell positions does not significantly affect the results. Moreover, a study of the grid sensitivity demonstrates that meshes with grid spacings of $\Delta x^+ = 300$, $\Delta y^+ = 100$, and $\Delta z^+ = 50$ are sufficiently refined to correctly predict the mean velocity and the turbulent intensities in the channel. Finally, the results obtained in the simulation performed for isothermal walls demonstrate the ability of wall-modeled LES to estimate thermal effects. Reliable results are thus expected when using the wall modeling approach in order to simulate more complex flow configurations, such as the development of a turbulent jet flow in the vicinity of the nozzle.

Appendix: Grid Sensitivity in Wall-Resolved Simulations

In Sec. II.B, a turbulent channel flow at $Re_\tau = 395$ has been simulated to evaluate the performance of the numerical algorithm. The influence of the spatial resolution of the channel on the LES

Table A1 Grid parameters to simulate a turbulent channel flow at $Re_\tau = 395$

LES	$n_x \times n_y \times n_z$	Δx^+	Δz^+	Δy_w^+	$\Delta y_{\max}^+$
Mesh M1	$101 \times 181 \times 121$	25	10	1	8
Mesh M2	$161 \times 181 \times 121$	15	10	1	8
Mesh M3	$161 \times 181 \times 241$	15	5	1	8

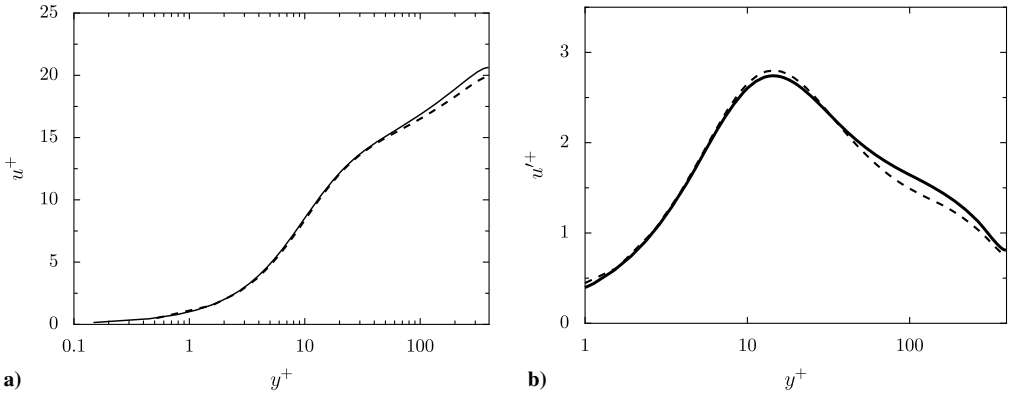

Fig. A1 Representations of a) mean and b) rms streamwise velocity profiles: LESs using mesh M1 (dashed–dotted lines), M2 (dotted lines), M3 (dashed lines); and DNS of [24] (solid lines).

results is now examined by performing three simulations using different meshes: M1, M2, and M3. The grid parameters (namely, the numbers of mesh points n_x, n_y, and n_z in each direction) as well as the streamwise, normal, and spanwise grid spacings (Δx^+, Δy^+, and Δz^+) in wall units are given in Table A1. The LES using mesh M2 corresponds to the simulation presented in Sec. II.B.

In wall-normal direction y, meshes M1, M2, and M3 are identical. In particular, at the wall, the grid spacing Δy_w^+ is equal to one. Further from the wall, the mesh is stretched in the y direction to obtain $\Delta y_{\max}^+ = 8$ at the center of the channel. In the streamwise and the spanwise directions, the grid spacings are uniform. They are equal to $\Delta x^+ = 25$ and $\Delta z^+ = 10$ in mesh M1, $\Delta x^+ = 15$ and $\Delta z^+ = 10$ in mesh M2, and $\Delta x^+ = 15$ and $\Delta z^+ = 5$ in mesh M3. The initial conditions and the procedure used to compute the statistical results are identical for the three computations. They are reported in Sec. II.B.3.

The mean longitudinal velocity profiles u^+ are displayed in wall units in Fig. A1a as a function of the wall distance y^+. For the three LESs, the agreement with the DNS is satisfactory in the inner region of the boundary layer for $y^+ \leq 20$. For values of $y^+ > 20$, discrepancies are observed between the profile of the LES using grid M1 and the DNS profile. For higher mesh resolution, differences between the LES and the DNS results are reduced. In particular, the LES performed with grid M3 provides a good agreement with the DNS.

The rms profiles for the streamwise velocity component u'^+, obtained in the three LESs and in the DNS of Abe et al. [24], are represented in Fig. A1b in wall units. In the LES using mesh M1, the amplitude of the peak is overestimated compared to the DNS results. The LES using refined grids M2 and M3 provide rms velocity profiles in better agreement with the DNS profile. In this case, the intensity of the rms peak is correctly estimated using the finest mesh, M3. These results demonstrate that the successive grid refinements in directions x and z allow the differences between the LES and the DNS to be reduced. In addition, using grid M3, one can note that increasing the grid resolution in direction z significantly improves the agreement with the DNS for both rms and mean velocity profiles.

Acknowledgments

This study is financially supported by Airbus. The postprocessing was performed using Antares.

References

[1] Colonius, T., and Lele, S. K., "Computational Aeroacoustics: Progress on Nonlinear Problems of Sound Generation," *Progress in Aerospace Sciences*, Vol. 40, No. 6, 2004, pp. 345–416. doi:10.1016/j.paerosci.2004.09.001

[2] Choi, H., and Moin, P., "Grid-Point Requirements for Large Eddy Simulation: Chapman's Estimates Revisited," *Center for Turbulence Research Annual Research Briefs*, Stanford Univ. Stanford, CA, 2011, pp. 31–36.

[3] Piomelli, U., and Balaras, E., "Wall-Layer Models for Large-Eddy-Simulations," *Annual Review of Fluid Mechanics*, Vol. 34, No. 1, 2002, pp. 349–374. doi:10.1146/annurev.fluid.34.082901.144919

[4] Deardorff, J. W., "A Numerical Study of Three-Dimensional Turbulent Channel Flow at Large Reynolds Numbers," *Journal of Fluid Mechanics*, Vol. 41, No. 2, 1970, pp. 453–480. doi:10.1017/S0022112070000691

[5] Schumann, U., "Subgrid Scale Model for Finite Difference Simulations of Turbulent Flows in Plane Channels and Annuli," *Journal of Computational Physics*, Vol. 18, No. 4, 1975, pp. 376–404. doi:10.1016/0021-9991(75)90093-5

[6] Slotnick, J., Khodadoust, A., Alonso, J., Darmofal, D., Gropp, W., Lurie, E., and Mavriplis, D., "CFD Vision 2030 Study: A Path to Revolutionary Computational Aerosciences," NASA CR-2014-218178, 2014.

[7] Kawai, S., and Larsson, J., "Wall-Modeling in Large Eddy Simulation: Length Scales, Grid Resolution, and Accuracy," *Physics of Fluids*, Vol. 24, No. 1, 2012, Paper 015105. doi:10.1063/1.3678331

[8] Lodato, G., Castonguay, P., and Jameson, A., "Structural Wall-Modeled LES Using a High-Order Spectral Difference Scheme for Unstructured Meshes," *Flow, Turbulence and Combustion*, Vol. 92, Nos. 1–2, 2014, pp. 579–606. doi:10.1007/s10494-013-9523-3

[9] Bocquet, S., Sagaut, P., and Jouhaud, J., "A Compressible Wall Model for Large-Eddy Simulation with Application to Prediction of Aerothermal Quantities," *Physics of Fluids*, Vol. 24, No. 6, 2012, Paper 065103. doi:10.1063/1.4729614

[10] Cambier, L., Heib, S., and Plot, S., "The Onera Elsa CFD Software: Input from Research and Feedback from Industry," *Mechanics and Industry*, Vol. 14, No. 3, 2013, pp. 159–174. doi:10.1051/meca/2013056

[11] Fosso, A., Deniau, H., Sicot, F., and Sagaut, P., "Curvilinear Finite Volume Scheme Using High Order Compact Intepolation," *Journal of Computational Physics*, Vol. 229, No. 13, 2010, pp. 5090–5122. doi:10.1016/j.jcp.2010.03.027

[12] Lele, S. K., "Compact Finite Difference Schemes with Spectral-Like Resolution," *Journal of Computational Physics*, Vol. 103, No. 1, 1992, pp. 16–42. doi:10.1016/0021-9991(92)90324-R

[13] Visbal, M. R., and Gaitonde, D. V., "On the Use of Higher-Order Finite-Difference Schemes on Curvilinear and Deforming Meshes," *Journal of Computational Physics*, Vol. 181, No. 1, 2002, pp. 155–185. doi:10.1006/jcph.2002.7117

[14] Bogey, C., and Bailly, C., "Computation of a High Reynolds Number Jet and Its Radiated Noise Using Large Eddy Simulation Based on Explicit Filtering," *Computers and Fluids*, Vol. 35, No. 10, 2006, pp. 1344–1358. doi:10.1016/j.compfluid.2005.04.008

[15] Fauconnier, D., Bogey, C., and Dick, E., "On the Performance of Relaxation Filtering for Large-Eddy Simulation," *Journal of Turbulence*, Vol. 14, No. 1, 2013, pp. 22–49. doi:10.1080/14685248.2012.740567

[16] Kremer, F., and Bogey, C., "Large-Eddy Simulation of Turbulent Channel Flow Using Relaxation Filtering: Resolution Requirement and Reynolds Number Effects," *Computers and Fluids*, Vol. 116, Aug. 2015,

pp. 17–28.
doi:10.1016/j.compfluid.2015.03.026
[17] Lazareff, M., Vuillot, A. M., and Cambier, L., "elsA Theoretical Manual," Ver. 2.1, Reference /ELSA/STB-97020, Property of ONERA, 2010.
[18] Bogey, C., and Bailly, C., "A Family of Low Dispersive and Low Dissipative Explicit Schemes for Flow and Noise Computations," *Journal of Computational Physics*, Vol. 194, No. 1, 2004, pp. 194–214. doi:10.1016/j.jcp.2003.09.003
[19] Fosso, A., Deniau, H., Lamarque, N., and Poinsot, T., "Comparison of Outflow Boundary Conditions for Subsonic Aeroacoustic Simulations," *International Journal for Numerical Methods in Fluids*, Vol. 68, No. 10, 2012, pp. 1207–1233. doi:10.1002/fld.v68.10
[20] Fosso Pouangué, A., Sanjosé, M., Moreau, S., Daviller, G., and Deniau, H., "Subsonic Jet Noise Simulations Using Both Structured and Unstructured Grids," *AIAA Journal*, Vol. 53, No. 1, 2015, pp. 55–69. doi:10.2514/1.J052380
[21] Carpenter, M. H., Gottlieb, D., and Abarbanel, S., "Time-Stable Boundary Conditions for Finite-Difference Schemes Solving Hyperbolic Systems: Methodology and Application to High-Order Compact Schemes," *Journal of Computational Physics*, Vol. 111, No. 2, 1994, pp. 220–236. doi:10.1006/jcph.1994.1057
[22] Sengupta, T. K., Ganeriwal, G., and De, S., "Analysis of Central and Upwind Compact Schemes," *Journal of Computational Physics*, Vol. 192, No. 2, 2003, pp. 677–694. doi:10.1016/j.jcp.2003.07.015
[23] Abe, H., Kawamura, H., and Matsuo, Y., "Direct Numerical Simulation of a Fully Developed Turbulent Channel Flow with Respect to the Reynolds Number Dependence," *Journal of Fluids Engineering*, Vol. 123, No. 2, 2001, pp. 382–393. doi:10.1115/1.1366680
[24] Abe, H., Kawamura, H., and Choi, H., "Very Large-Scale Structures and Their Effects on the Wall Shear-Stress Fluctuations in a Turbulent Channel Flow up to $Re_\tau = 60$," *Journal of Fluids Engineering*, Vol. 126, No. 5, 2004, pp. 835–843. doi:10.1115/1.1789528
[25] Moser, R. D., Kim, J., and Mansour, N. N., "Direct Numerical Simulation of Turbulent Channel Flow up to $Re_\tau = 560$," *Physics of Fluids*, Vol. 11, No. 4, 1999, pp. 943–945. doi:10.1063/1.869966
[26] Cabrit, O., "Direct Simulations for Wall Modeling of Multicomponent Reacting Compressible Turbulent Flows," *Physics of Fluids*, Vol. 21, No. 5, 2009, Paper 055108. doi:10.1063/1.3123528
[27] Kremer, F., "Étude Numérique D'Écoulements de Paroi Compressibles: Méthodes D'Intégration Temporelle Semi-Implicites et Application du Canal Plan Turbulent," Ph.D. Thesis, École Centrale de Lyon, Lyon, France, 2012.
[28] Reichardt, H., "The Fundamentals of Turbulent Heat Transfer," *Archiv fuer die Gesamte Waermetechnik, (West Germany)*, Vol. 6, Nos. 6/7, 1951, pp. 129–143.
[29] Kader, B. A., "Temperature and Concentration Profiles in Fully Turbulent Boundary Layers," *International Journal of Heat and Mass Transfer*, Vol. 24, No. 9, 1981, pp. 1541–1544. doi:10.1016/0017-9310(81)90220-9
[30] van Driest, E. R., "Turbulent Boundary Layer in Compressible Fluids," *Journal of the Aeronautical Sciences*, Vol. 18, No. 3, 1951, pp. 145–160. doi:10.2514/8.1895
[31] Aikens, K. M., Dhamankar, N. S., Martha, C. S., Yingchong, S., Blaisdell, G. A., Lyrintzis, A. S., and Li, Z., "Equilibrium Wall Model for Large Eddy Simulations of Jets for Aeroacoustics," *AIAA SciTech, 52nd Aerospace Sciences Meeting*, AIAA Paper 2014-0180, 2014.
[32] Hoyas, S., and Jiménez, J., "Scaling of the Velocity Fluctuations in Turbulent Channels up to $Re_\tau = 2003$," *Physics of Fluids*, Vol. 18, No. 1, 2006, Paper 011702. doi:10.1063/1.2162185
[33] Sleicher, C. A., and Rouse, M. W., "A Convenient Correlation for Heat Transfer to Constant and Variable Property Fluids in Turbulent Pipe Flow," *International Journal of Heat and Mass Transfer*, Vol. 18, No. 5, 1975, pp. 677–683. doi:10.1016/0017-9310(75)90279-3
[34] Bodart, J., and Larsson, J., "Wall-Modeled Large Eddy Simulation in Complex Geometries with Application to High-Lift Devices," Center for Turbulence Research, Annual Research Briefs, Stanford Univ., Stanford, CA, 2011, pp. 37–48.
[35] Lee, J., Cho, M., and Choi, H., "Large Eddy Simulations of Turbulent Channel and Boundary Layer Flows at High Reynolds Number with Mean Wall Shear Stress Boundary Conditions," *Physics of Fluids*, Vol. 25, No. 11, 2013, Paper 110808.
[36] Park, G. I., and Moin, P., "An Improved Dynamic Non-Equilibrium Wall-Model for Large Eddy Simulation," *Physics of Fluids*, Vol. 26, No. 1, 2014, Paper 015108. doi:10.1063/1.4861069
[37] Petukhov, B. S., "Heat Transfer and Friction in Turbulent Pipe Flow with Variable Physical Properties," *Advances in Heat Transfer*, Vol. 6, 1970, pp. 503–564. doi:10.1016/S0065-2717(08)70153-9

M. R. Visbal
Associate Editor